Elementary processes in dilatational plasticity of glasses

Avraham Moriel,[1] David Richard,[2] Edan Lerner,[3] and Eran Bouchbinder[1]
[1]*Chemical and Biological Physics Department, Weizmann Institute of Science, Rehovot 7610001, Israel*
[2]*Université Grenoble Alpes, CNRS, LIPhy, 38000 Grenoble, France*
[3]*Institute for Theoretical Physics, University of Amsterdam, Science Park 904, Amsterdam, Netherlands*

(Received 5 February 2024; accepted 30 April 2024; published 13 May 2024)

Materials typically fail under complex stress states, essentially involving dilatational (volumetric) components that eventually lead to material decohesion/separation. It is therefore important to understand dilatational irreversible deformation—i.e., dilatational plasticity—en route to failure. In the context of glasses, much focus has been given to shear (volume-preserving) plasticity, both in terms of the stress states considered and the corresponding material response. Here, using a recently developed methodology and extensive computer simulations, we shed basic light on the elementary processes mediating dilatational plasticity in glasses. We show that plastic instabilities, corresponding to singularities of the glass Hessian, generically feature both dilatational and shear irreversible strain components. The relative magnitude and statistics of the strain components depend both on the symmetry of the driving stress (e.g., shear versus hydrostatic tension) and on the cohesive (attractive) part of the interatomic interaction. We further show that the tensorial shear component of the plastic strain is generally nonplanar and also extract the characteristic volume of plastic instabilities. Elucidating the fundamental properties of the elementary micromechanical building blocks of plasticity in glasses sets the stage for addressing larger-scale, collective phenomena in dilatational plasticity such as topological changes in the form of cavitation and ductile-to-brittle transitions. As a first step in this direction, we show that the elastic moduli markedly soften during dilatational plastic deformation approaching cavitation.

DOI: 10.1103/PhysRevResearch.6.023167

I. INTRODUCTION

Glassy materials are ubiquitous in the natural and technological world around us, and include various noncrystalline solids such as oxide glasses, glassy polymers, organic glasses and metallic glasses. These intrinsically disordered materials possess notable properties and hence find an enormous range of engineering applications [1–5]. Processing glassy materials [6] and more so their performance, durability and structural integrity in various applications require deep and fundamental understanding of their mechanical deformation and failure modes. Failure typically involves complex stress states, essentially involving dilatational (volumetric) components that eventually lead to material decohesion/separation. This is evident from extensive experimental observations regarding cavitation in glasses under a wide variety of failure conditions (e.g., Refs. [7–16]).

Despite its crucial importance, our current understanding of irreversible (plastic) dilatational deformation of glasses lags far behind the corresponding understanding of shear (deviatoric, volume-preserving) plasticity. Indeed, a lot of attention and research effort have been devoted to studying the fundamental micromechanics and statistical-mechanical properties of shear plasticity—especially in the statistical physics community (e.g., Refs. [17–36]), with a few notable recent counterexamples (e.g., Refs. [37–45]). The meaning of "shear plasticity" here is two-fold; first, it refers to shear-driven plasticity, i.e., to studying plasticity under *driving conditions* (stress states) in which the shear/deviatoric component strongly dominates the dilatational/volumetric one. Second, it refers to the irreversible *material response*, which in previous works heavily focused on plastic shear strains mediated by the so-called shear transformation zones (STZs) [46–49].

The pressing need to understand dilatational plasticity processes has already been recognized in several materials research communities, mainly in the context of metallic glasses [7–16,50,51], leading to various experimental (e.g., Refs. [8,9]), simulational (e.g., Refs. [50,51]) and modeling (e.g., Refs. [51,52]) efforts. It has also given rise to the conjecture that at the fundamental level there exist in addition to STZs (the carriers of shear plasticity) also tension-transformation zones (TTZs) [8,9,53], whose activation leads to atomic-scale quasicleavage [54]. Yet, these important efforts have not been focused on the basic micromechanics, geometry, and statistical mechanics of dilatational plasticity.

Our goal in this work is to study the fundamental micromechanics, geometric, and statistical-mechanical properties of the elementary processes that mediate dilatational plasticity in glasses. In terms of driving forces, we invoke the hydrostatic tension test and compare it to its well-studied simple shear counterpart, both shown in Fig. 1. The hydrostatic tension test applied to computer glass samples physically represents a mesoscopic portion of a macroscopic glass, on which the

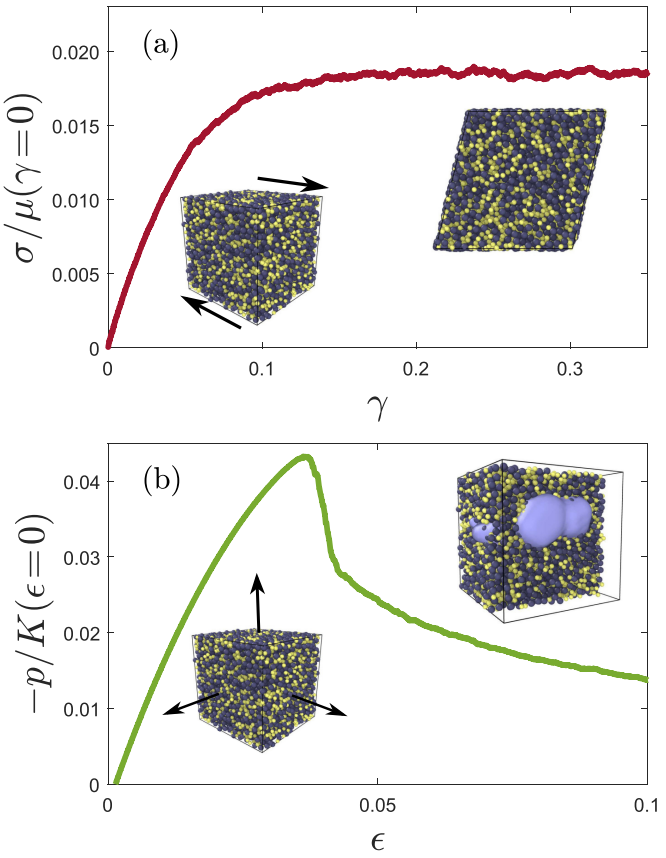

FIG. 1. (a) A shear stress-strain $\sigma(\gamma)$ of a 3D computer glass (of $N=10K$ particles, averaged over 108 realizations) deformed under simple shear. σ is normalized by the initial shear modulus, $\mu(\gamma=0)$. The left inset shows the binary-mixture glass (blue and yellow particles correspond to the two species [55]) prior to deformation and the arrows illustrate the subsequent application of simple shear. The right inset shows a side view of the same glass realization in the steady-state flow regime (here $\gamma\simeq 0.25$). (b) The corresponding dilatational stress-strain $-p(\epsilon)$ for the same glass ensemble (p is the pressure) deformed under hydrostatic tension. $-p$ is normalized by the initial bulk modulus, $K(\epsilon=0)$. The left inset shows the very same undeformed glass realization as in panel (a), but the arrows highlight the subsequent application of hydrostatic tension (pure dilation). The right inset shows a large-scale cavity (light blue region) inside the glass right after the observed abrupt stress drop. See text for a discussion of the results.

surrounding material exerts predominantly hydrostatic forces. In Fig. 1(a), an ensemble-averaged shear stress-strain curve under simple shear is presented, obtained through 3D computer simulations using athermal quasistatic (AQS) deformation [17–20]. The resulting curve features a small-strain linear regime and a smooth, monotonic transition to a steady-state flow plateau upon shear plastic yielding. The curve does not feature a stress overshoot (and the accompanying stress drop), a situation that is typical for poorly annealed (i.e., rapidly quenched) glasses, which indeed corresponds to the employed glass ensemble [55].

In Fig. 1(b), an ensemble-averaged dilatational stress-strain curve under hydrostatic tension (pure dilation) is presented, obtained using the very same ensemble of computer glasses as in panel (a). The resulting curve features a small-strain linear regime, followed by an abrupt stress drop and continuous strain softening. It qualitatively differs from its simple shear counterpart in Fig. 1(a), despite performing the deformation simulations on the very same ensemble of glass realizations. One manifestation of this qualitative difference is the emergence of a cavitation instability in the hydrostatic tension test, as illustrated in the inset (see figure caption for additional details). A major goal of this work is to study the elementary irreversible processes that contribute to the observed differences.

Our methodology, involving computer glasses of N particles and initial volume V_0, is discussed in Appendix A, where additional technical details are provided in [55]. As material cohesion is essential for understanding dilatational plasticity and failure, our computer simulations employ a class of recently introduced potentials, which feature both repulsion and cohesion/attraction, where the strength of the attractive part is continuously adjustable through a dimensionless parameter r_c [55–58]. The smaller r_c is, the stronger the cohesive/attractive part of the interaction, as demonstrated in the inset of Fig. 2(a). It was recently shown that reducing r_c can lead to a ductile-to-brittle transition [34].

Simple shear AQS deformation in a given direction is controlled by a shear strain γ, where a representative simple shear stress-strain curve $\sigma(\gamma)$ is presented in Fig. 1(a). Hydrostatic tension (pure dilation) is controlled by a dilatational (volumetric) strain ϵ, representative hydrostatic tension stress-strain curve $-p(\epsilon)$ is presented in Fig. 1(b) (p is the hydrostatic pressure). Unstable plastic eigenmodes $\boldsymbol{u}(\boldsymbol{r})$ (where $\boldsymbol{r}$ is a position vector relative to the center of the eigenmode [55]), corresponding to a zero crossing of an eigenvalue of the Hessian $\boldsymbol{M}$, are identified during AQS deformation, controlled either by γ or ϵ (see Appendix A and [55]). $\boldsymbol{u}(\boldsymbol{r})$ features a highly nonlinear, disordered core of linear size a (i.e., of volume $\mathcal{V}\propto a^3$) and a power-law decay $|\boldsymbol{r}|^{-2}$ in the far field (e.g., [20]), $|\boldsymbol{r}|\gg a$, associated with a linear elastic continuum behavior.

The irreversible deformation inside the nonlinear core is quantified through an eigenstrain tensor $\boldsymbol{\mathcal{E}}^*$ in the framework of Eshelby's inclusions formalism [59,60]. A recently developed method [61], based on a class of contour integrals evaluated in the far field $|\boldsymbol{r}|\gg a$, allows to extract $\mathcal{V}\boldsymbol{\mathcal{E}}^*$. Our primary goal is to study the properties of $\boldsymbol{\mathcal{E}}^*$ and $\mathcal{V}$ (or alternatively a) as a function of the symmetry and magnitude of the driving force, quantified by γ and ϵ, and as a function of the strength of the cohesive/attractive part of the interatomic interaction, quantified by r_c.

II. PLASTIC EIGENSTRAIN TRIAXILITY

The eigenstrain tensor can be additively decomposed into its dilatational (volumetric) part $\boldsymbol{\mathcal{E}}^*_{\rm dil}$ and deviatoric (shear, volume-preserving) part $\boldsymbol{\mathcal{E}}^*_{\rm dev}$, $\boldsymbol{\mathcal{E}}^*=\boldsymbol{\mathcal{E}}^*_{\rm dil}+\boldsymbol{\mathcal{E}}^*_{\rm dev}$. In 3D, $\boldsymbol{\mathcal{E}}^*$ is characterized by three independent amplitudes, one characterizing the dilatational (isotropic) part, $\boldsymbol{\mathcal{E}}^*_{\rm dil}=\epsilon^*_{\rm dil}\boldsymbol{\mathcal{I}}$ and two characterizing the deviatoric part, which features $\mathrm{tr}(\boldsymbol{\mathcal{E}}^*_{\rm dev})=0$. We denote by $\epsilon^*_{\rm dev,1}$ the largest (in absolute value) of the three eigenvalues of $\boldsymbol{\mathcal{E}}^*_{\rm dev}$ and by $\epsilon^*_{\rm dev,2}$ the second largest, which has a different sign compared to $\epsilon^*_{\rm dev,1}$ (the third

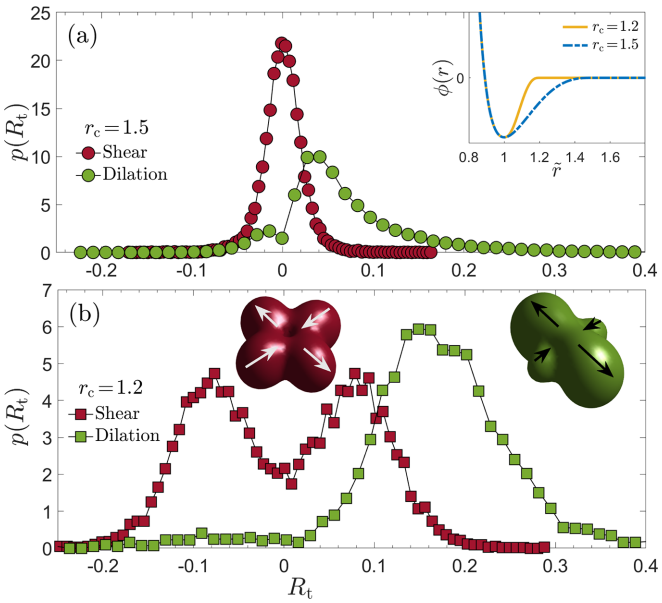

FIG. 2. (a) The probability distribution $p(R_t)$ of the plastic eigenstrain triaxiliaty R_t defined in Eq. (1) for $r_c = 1.5$ glasses, under both simple shear and hydrostatic tension (see legend). The inset presents the interatomic pair interaction $\phi(r)$ vs $\tilde{r}$, where r is the scaled distance between interacting particles and $\tilde{r}$ is further normalized such that the minimum of each curve occurs at $\tilde{r} = 1$ [55,57]. Curves for the two values of r_c employed in this work (see legend) are shown. (b) The same as (a), but for $r_c = 1.2$. See text for an extensive discussion of the results. The visual insets present isosurfaces of the magnitude of plastic modes with two values of R_t. The left one (red), corresponds to $R_t = 0$ (i.e., $\epsilon^*_{dil} = 0$) and a planar deviatoric eigenstrain tensor with $J^*_2 = 1$. The effective dimensionality of the deviatoric eigenstrain tensor (quantifying its degree of planarity) is discussed in relation to Fig. 3. The arrows (white) indicate the direction of the displacement (with length that is consistent with its magnitude). The right visual inset (green) corresponds to $\epsilon^*_{dil} = 0.5$ and again a planar deviatoric eigenstrain tensor with $J^*_2 = 1$, resulting in $R_t \simeq 0.29$. The arrows (black) indicate the direction of the displacement (with length that is consistent with its magnitude).

eigenvalue is not independent, but is rather determined through $\mathrm{tr}(\boldsymbol{\mathcal{E}}^*_{dev}) = 0$).

Three independent amplitudes that characterize $\boldsymbol{\mathcal{E}}^*$ provide basic information about the geometry of plastic rearrangements/instabilities in glasses. Of particular interest in the present context is the amplitude of the dilatational eigenstrain component ϵ^*_{dil}, and more specifically its relative magnitude compared to the deviatoric component. Consequently, we aim at constructing a ratio of the two components in order to quantify their relative magnitude. This goal naturally fits the contour integrals method [61] that—as noted above—allows to extract only the product $\mathcal{V}\boldsymbol{\mathcal{E}}^*$, but not $\mathcal{V}$ and $\boldsymbol{\mathcal{E}}^*$ individually. In fact, as $\boldsymbol{u}(\boldsymbol{r})$ is a normalized mode (by construction), considering absolute eigenstrain values is not immediate. Yet, as will be shown later, the fully nonlinear $\boldsymbol{u}(\boldsymbol{r})$ does contain information that allows to estimate the core volume $\mathcal{V}$.

In order to construct a ratio that quantifies the relative magnitude of the dilatational and deviatoric components of the eigenstrain tensor $\boldsymbol{\mathcal{E}}^*$, we draw analogy with the well-known and widely used stress triaxiality measure [62,63]—constructed at the macroscopic scale for a similar goal, but with respect to the stress tensor—and define

$$R_t \equiv \frac{\epsilon^*_{dil}}{\sqrt{3J^*_2}}, \tag{1}$$

where $J^*_2 \equiv \frac{1}{2}\boldsymbol{\mathcal{E}}^*_{dev} : \boldsymbol{\mathcal{E}}^*_{dev}$. We term the ratio R_t in Eq. (1) the plastic eigenstrain triaxiality. Note that R_t is a signed quantity, as will be further discussed below.

In Fig. 2, the probability distribution $p(R_t)$ is plotted for both the simple shear and hydrostatic tension tests, and two values of r_c. $p(R_t)$ was obtained by calculating R_t of Eq. (1) for 200 independent glass samples (made of $N = 128$ K particles each) per r_c value, where for each sample up to the first 50 plastic instabilities/events were detected [55]. Under dilation, we focused on strains below the cavitation strain [corresponding to the peak stress under hydrostatic tension, cf. Fig. 1(b)], implying that not all of the detected plastic events were analyzed. Overall, the presented distributions were generated using between 3000 and 10 000 events each. Statistical convergence and possible effects of the magnitude of the applied strain are discussed in Ref. [55], also for other observables to be considered below.

In Fig. 2(a), we show $p(R_t)$ for $r_c = 1.5$, which corresponds to the canonical Lennard-Jones interatomic potential (see inset). It is observed that under simple shear (red circles) $p(R_t)$ is symmetric and narrowly peaked around $R_t = 0$ (i.e., a vanishing dilatational eigenstrain, $\epsilon^*_{dil} = 0$). Note that $\epsilon^*_{dil} > 0$ corresponds to isotropic core expansion/dilation and $\epsilon^*_{dil} < 0$ to isotropic core contraction [55]. It is observed that finite values of ϵ^*_{dil} exist, though R_t is small, indicating that the deviatoric eigenstrain component is significantly larger than the dilatational one. Under hydrostatic tension (green circles), for the very same ensemble of glass realizations, the symmetry between core expansion and contraction, $R_t \to -R_t$, is broken, and $p(R_t)$ is biased toward positive R_t values. $p(R_t)$ is peaked at relatively small values, again indicating a dominance of the deviatoric component over the dilatational one, even when the global driving force is dilatational (hydrostatic tension).

The results presented in Fig. 2(a) demonstrate that plastic instabilities in glasses generically feature both dilatational and shear components. A corollary of this finding is that at least part of dilatational plasticity is carried by the same micromechanical objects that carry shear plasticity. Moreover, the relative magnitude of the dilatational and deviatoric components depends on the stress state, i.e., the microscopic plastic strain is not an intrinsic/geometric property of plastic instabilities (for a given glass composition and interatomic interaction). Finally, hydrostatic tension gives rise to larger dilatational plastic strains, though for the canonical Lennard-Jones potential the deviatoric plastic strain is dominant.

We then repeated the calculations leading to Fig. 2(a) for an ensemble of glasses generated with $r_c = 1.2$. This value of r_c corresponds to an interatomic potential featuring a stronger cohesive/attractive part, see inset of Fig. 2(a). In the presence of stronger cohesion, one expects that in order to trigger an irreversible rearrangement, particles at the core of a plastic mode (saddle configuration) would feature a larger separation,

i.e., $p(R_t)$ is expected to feature larger values. The results in Fig. 2(b) support this expectation.

It is observed that under simple shear (red squares) $p(R_t)$ is still symmetric around $R_t = 0$, but becomes bimodal with peaks at R_t values significantly larger than the typical R_t values for $r_c = 1.5$ [cf. the red circles in Fig. 2(a)]. Moreover, this physical effect significantly intensifies under hydrostatic tension, as demonstrated by $p(R_t)$ in Fig. 2(b) (green squares). It is observed that under these conditions, $r_c = 1.2$ glasses feature almost only positive R_t values, and $p(R_t)$ is broad, where plastic events with a sizable dilatational component exist with a non-negligible probability. The geometry of plastic cores with different R_t values is illustrated in the visual insets of Fig. 2(b), see figure caption for details.

Overall, the results of Fig. 2 show that a dilatational plastic strain generically exists in plastic instabilities in glasses, along with a deviatoric plastic strain, and that their relative magnitude depends on both the driving conditions and the cohesive/attractive part of interatomic interactions. Moreover, our findings show that at least part of dilatational plasticity in glasses is carried by the same micromechanical objects that carry shear plasticity, and consequently that these provide a coupling mechanism between the two.

The generic existence of a dilatational plastic strain in plastic events in glasses has also been demonstrated previously in 2D Lennard-Jones glasses studied under uniaxial tension/compression [64] and under simple shear [65], and in 3D computer models of amorphous silicon studied under simple shear [66]. Amorphous silicon has been modelled in [66] using either the standard/original Stillinger-Weber (SW) potential [67] or a modified SW (termed SWM therein) potential [68,69]. The latter potential, which features a three-body term twice as large as the original SW potential, has been developed in relation to the fracture of crystalline silicon, where it was found that the SW potential leads to a ductile behavior, while the SWM potential to a brittle one [68,69]. This is reminiscent of the ductile-to-brittle transition induced by reducing r_c, as discussed in Ref. [34]. The ductile-to-brittle transition in both cases is also accompanied by a reduction in Poisson's ratio (see Table I in Ref. [66] for the SW and SWM values, and Table S2 in Ref. [55] for the different r_c values).

Interestingly, it was reported in [66] (cf. Fig. 7 therein) that the relative magnitude of the dilatational and deviatoric components of plastic events under simple shear (termed "shear-tension coupling") increases from SW to SWM. This is precisely the trend observed in Fig. 2 (red symbols in the two panels) with decreasing r_c. Consequently, while "ductility" and "brittleness" are clearly collective phenomena that are affected by both the history dependence of a glass (i.e., its initial state of disorder emerging from the quench self-organization, being in itself affected by the interatomic potential) and by spatiotemporal interactions of an extensive number of plastic events during deformation [16,34], they might also have some signature in the geometry of individual plastic events.

III. PLANARITY OF THE DEVIATORIC EIGENSTRAIN TENSOR

The plastic eigenstrain triaxility R_t, studied above, constructs out of the three independent amplitudes that characterize the eigenstrain tensor $\boldsymbol{\mathcal{E}}^*$ a measure of the relative magnitude of the dilatational and deviatoric eigenstrain components. Next, we consider another geometric property of the core of plastic instabilities. As the dilatational component is isotropic, i.e., it features 3D spherical geometry, we focus our attention on the geometry of the deviatoric eigenstrain tensor $\boldsymbol{\mathcal{E}}^*_{\rm dev}$, which is characterized by two independent amplitudes $\epsilon^*_{{\rm dev},1}$ and $\epsilon^*_{{\rm dev},2}$, defined above.

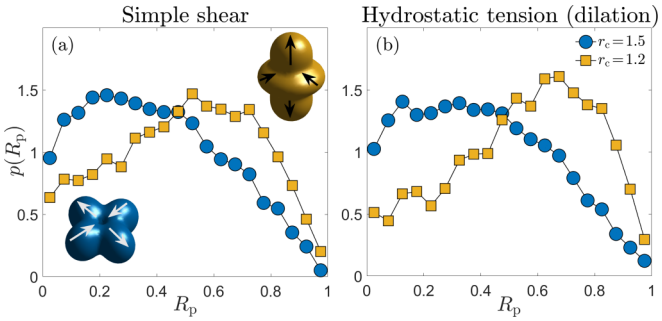

FIG. 3. The probability distribution $p(R_p)$ of the planarity ratio R_p of the deviatoric eigenstrain tensor, cf. Eq. (2), in glasses under simple shear, for two values of r_c (see legend in panel (b)). The visual insets present iso-surfaces of the magnitude of the deviatoric part of plastic modes with two values of R_p. The left one (blue), corresponds to $R_p = 0$ (i.e., the purely planar limit), and is identical to the left visual inset in Fig. 2(b). The right visual inset (yellow), corresponds to $R_p = 1$ (i.e., the least planar). In both cases, the arrows indicate the direction of the displacement (with length that is consistent with its magnitude). (b) The same as panel (a), but under hydrostatic tension. See text for a discussion.

A lot of previous insight into glass plasticity has been gained using computer simulations in 2D, which—as highlighted above—focused mostly on shear plasticity. In 2D, the deviatoric eigenstrain tensor is characterized by a single independent amplitude. There were some preliminary indications in the literature that plastic instabilities in 3D feature such a planar deviatoric eigenstrain tensor as well (e.g., Ref. [70]). That is, in terms of the above-defined quantities, it was suggested that $\epsilon^*_{{\rm dev},1} \simeq -\epsilon^*_{{\rm dev},2}$ (such that the magnitude of the third eigenstrain is much smaller than $|\epsilon^*_{{\rm dev},1}|$) also characterizes plastic instabilities in 3D. Yet, to the best of our knowledge, this issue has not been systematically investigated in the past.

To address this basic issue, we define the planarity ratio of the deviatoric eigenstrain tensor $\boldsymbol{\mathcal{E}}^*_{\rm dev}$ of plastic instabilities as

$$R_p \equiv 2\left(1 + \frac{\epsilon^*_{{\rm dev},2}}{\epsilon^*_{{\rm dev},1}}\right). \tag{2}$$

As explained above, in the purely planar limit one eigenvalue of $\boldsymbol{\mathcal{E}}^*_{\rm dev}$ vanishes and we have $\epsilon^*_{{\rm dev},1} = -\epsilon^*_{{\rm dev},2}$, i.e., $R_p = 0$. The opposite limit, the least planar one, corresponds to $\epsilon^*_{{\rm dev},2}/\epsilon^*_{{\rm dev},1} = -1/2$, i.e., $R_p = 1$. These limiting cases are illustrated in the visual insets in Fig. 3(a) (see figure caption for additional details). In these terms, the suggestion that the deviatoric eigenstrain tensor remains planar in 3D corresponds to $p(R_p) \to \delta(R_p)$, i.e., to a probability distribution $p(R_p)$ that is strongly concentrated near the planar limit $R_p \simeq 0$, approaching a delta-function distribution. Our goal

is to study $p(R_p)$ as a function of the external driving force (simple shear vs hydrostatic tension) and r_c. The analysis was performed on the same set of plastic instabilities/events discussed in relation to Fig. 2, and the results are presented in Fig. 3. In Fig. 3(a), $p(R_p)$ under simple shear is plotted for two values of r_c [those previously used in Fig. 2, see legend in Fig. 3(b)]. It is observed that for $r_c = 1.5$, $p(R_p)$ features a broad peak around $R_p \simeq 0.3$, significantly deviating from $\delta(R_p)$. Moreover, for $r_c = 1.2$ (corresponding to a stronger attractive part of the interatomic potential), $p(R_p)$ is also broad, but is peaked at significantly larger values of R_p, away from the planar limit. The corresponding results under hydrostatic tension are presented in Fig. 3(b) and are similar [note that $p(R_p)$ is more sharply peaked around $R_p \simeq 0.7$ compared to the corresponding result under simple shear, cf. panel (a)]. Overall, the results indicate that the geometry of the deviatoric eigenstrain tensor $\boldsymbol{\mathcal{E}}^*_{\rm dev}$ is generally nonplanar, i.e., that the dimensionality of $\boldsymbol{\mathcal{E}}^*_{\rm dev}$ is the same as space dimensionality.

IV. THE CORE SIZE OF PLASTIC INSTABILITIES

As pointed out above, the contour integrals method, which employs the far field linear elastic properties of unstable plastic modes $\boldsymbol{u}(\boldsymbol{r})$ to infer the core properties, does not allow to separately extract the core volume $\mathcal{V}$ and plastic eigenstrain tensor $\boldsymbol{\mathcal{E}}^*$. Yet, the core volume $\mathcal{V}$—or equivalently the linear core size a (with $\mathcal{V} \propto a^3$)—is an important glassy length scale. For example, it has been argued that $\mathcal{V}$ influences various physical properties of glasses [71–73]. Consequently, it is important to extract $\mathcal{V} \propto a^3$ itself. In fact, the particle-level (atomistic), fully nonlinear $\boldsymbol{u}(\boldsymbol{r})$ can be used to estimate a.

The unstable plastic mode displacement field $\boldsymbol{u}(\boldsymbol{r})$ is evaluated at each spatial position $\boldsymbol{r}_i$ occupied by a particle, hence it can be denoted as $\boldsymbol{u}_i \equiv \boldsymbol{u}(\boldsymbol{r}_i)$ (which is the quantity we actually calculate to begin with). $\boldsymbol{u}_i$ follows a continuum linear elastic behavior for $|\boldsymbol{r}_i| \gg a$, yet it features significant nonlinearity and larger displacements over shorter distances. A widely used measure of spatial localization is the participation number (i.e., the participation ratio multiplied by N) $(\sum_i |\boldsymbol{u}_i|^2)^2 / \sum_i |\boldsymbol{u}_i|^4$ [74,75], which is $\mathcal{O}(1)$ in the extreme localization limit and $\mathcal{O}(N)$ in the spatially extended limit. Consequently, the participation number provides an estimate for the number of particles inside the core of $\boldsymbol{u}_i$, and we estimate the dimensionless core size as

$$\frac{a}{a_0} \equiv \left(\frac{1}{\sum_i |\boldsymbol{u}_i|^4} \right)^{1/3}. \tag{3}$$

Here, $a_0 \equiv (V_0/N)^{1/3}$ is a characteristic interparticle distance, $i = 1-N$ runs over all particles and we used the fact that unstable plastic modes are normalized by construction, i.e., $\sum_i |\boldsymbol{u}_i|^2 = 1$.

The probability distribution $p(a/a_0)$ is presented in Fig. 4 for two values of r_c, and under both simple shear and hydrostatic tension, for the plastic events previously analyzed in Figs. 2–3. In Fig. 4(a), we plot $p(a/a_0)$ under simple shear for both $r_c = 1.5$ (light blue circles) and $r_c = 1.2$ (yellow squares). It is observed that $p(a/a_0)$ is peaked at a few interparticle distances. Moreover, it shifts to larger values and becomes wider with increasing r_c. Note that in the definition in Eq. (3), we do not account for the increase in the volume per particle in dilation (but rather use the fixed linear size a_0) because over the range of dilatational strains we consider, the implied changes are small.

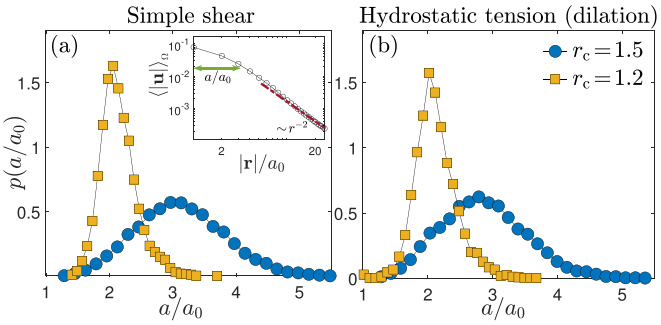

FIG. 4. (a) The probability distribution $p(a/a_0)$ of the dimensionless linear size a/a_0 of the core of unstable plastic modes, as defined in Eq. (3), for two values of r_c [see legend in (b)] under simple shear. (inset) The amplitude of an unstable plastic mode $\langle |\boldsymbol{u}| \rangle_\Omega$ [the solid angle Ω average of the norm of $\boldsymbol{u}(\boldsymbol{r})$] vs $|\boldsymbol{r}|/a_0$ in an $r_c = 1.5$ glass. The estimated core size a/a_0 is marked by the horizontal green double arrow and the linear elastic far-field power law $\sim 1/r^2$ is highlighted (red dashed-dotted line). (b) The same as (a), but under hydrostatic tension. See text for a discussion.

In Fig. 4(b), we present the corresponding results under hydrostatic tension, which are quantitatively similar to the simple shear results presented in panel (a). The inset in panel (a) shows an example of the amplitude of an unstable plastic mode $\langle |\boldsymbol{u}| \rangle_\Omega$ [the solid angle Ω average of the norm of $\boldsymbol{u}(\boldsymbol{r})$] as a function of $|\boldsymbol{r}|/a_0$. The estimated core size a/a_0 is marked by the horizontal green double arrow and the linear elastic far-field power-law $\sim r^{-2}$ is highlighted (red dashed-dotted line). The results of Fig. 4 show that the core size of plastic instabilities is nearly independent of the symmetry of the loading, but does depend on the interatomic interaction potential. Specifically, it becomes more compact with increasing attractive forces, i.e., decreasing r_c. This trend is also consistent with observed correlations between decreasing Poisson's ratio ν and the plastic core size (sometimes termed the STZ size/volume) [57,66,76], see the variation of ν with r_c in Table II of [55].

The characteristic core size a is similar to the core size ξ_g of quasilocalized, nonphononic modes in glasses [77–82]. Quasilocalized glassy modes, defined in the reference/undeformed glass, have been recently shown to follow a universal density of states $\sim \omega^4$ (distinct from Debye's density of states of low-frequency phonons, where ω is the vibrational frequency), and to feature a spatial structure similar to that of unstable plastic modes. In particular, quasilocalized modes are characterized by a nonlinear, disordered core of linear size ξ_g and a linear elastic power-law decay $|\boldsymbol{r}|^{-2}$ in the far field, $|\boldsymbol{r}| \gg \xi_g$, exactly like unstable plastic modes. Moreover, the trend of variation of a and ξ_g with varying r_c is similar (compare our results to Fig. 7(i) in Ref. [57]). Overall, our findings reinforce the suggestion that plastic instabilities are predominantly quasilocalized modes that are driven to a saddle-node bifurcation.

V. THE SOFTENING OF ELASTIC MODULI UNDER DILATATIONAL PLASTICITY

We provided above a basic quantitative characterization of the geometry and statistical-mechanical properties of the elementary micromechanical carriers of plasticity in glasses, for two end members of driving force symmetries (simple shear versus hydrostatic tension) and variable strength of cohesive/attractive interatomic interactions. In particular, the distributions of geometric properties (quantified by the ratios R_t and R_p) and a characteristic length (core size a) of plastic instabilities have been calculated. Our focus was on dilatational plasticity and its comparison to shear plasticity, both in terms of the driving forces and the material response manifested in the localization length a and the eigenstrain tensor $\mathcal{E}^*$.

The collective spatiotemporal accumulation of these elementary plasticity processes, including their coupling and emerging spatial organization, gives rise to larger-scale plasticity in glasses. Much of these collective phenomena, in relation to dilatational plasticity in particular, remain to be explored and understood. We stress (again) that we focused on unstable plastic modes and not on the outcome of the instabilities, and also note that we do not claim to have exhaustively identified all elementary dilatational plasticity processes in glasses. For example, we have not discussed microcavitation, i.e., the process by which cavities on the particle scale are formed [to be distinguished from the larger-scale cavitation observed in Fig. 1(b)]. These may be related to the micromechanical objects we identified (e.g., a subset of the outcomes of the identified plastic instabilities) or correspond to different objects. Yet, we would like to conclude this paper by demonstrating the type of new effects associated with collective dilatational plasticity.

We already demonstrated a qualitative difference between collective shear and dilatational elasto-plastic dynamics in Fig. 1, manifested at the level of stress-strain curves. Here, we provide another example, focusing on the strain evolution of elastic moduli, which can serve as global proxies for the structural changes experienced by a glass during elasto-plastic deformation. In Fig. 5, we present the strain evolution of the ensemble-averaged bulk modulus K and shear modulus μ, under simple shear and hydrostatic tension. We stress that K and μ, which characterize minima of the potential energy (see precise definitions in Ref. [55]), should not be confused with the tangent moduli, which characterize derivatives of the global, fluctuations averaged stress-strain curves. The two loading protocols are applied to the very same glass ensemble, composed of 200 samples generated with $N = 128$K and $r_c = 1.2$ (e.g., compared to $N = 10$K and $r_c = 1.5$ in Fig. 1), resulting in strains approaching the steady-state regime in the simple shear case and going beyond the stress drop in the hydrostatic tension case (cf. Fig. 1).

It is observed that under simple shear [Fig. 5(a)], both elastic moduli are largely unaffected by plastic deformation. In particular, the bulk modulus $K(\gamma)$ is essentially independent of γ and $\mu(\gamma)$ softens by $\sim$7% from the initial (as cast, undeformed) glass to the steady shear flow. The corresponding results under hydrostatic tension are presented in Fig. 5(b). First, it is observed that both moduli experience a large drop associated with large-scale cavitation [see Fig. 1(b)], here

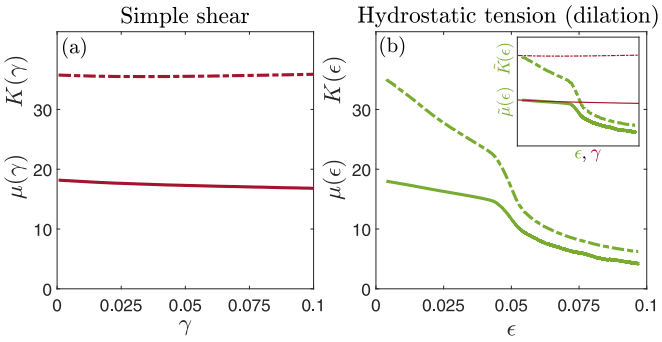

FIG. 5. (a) The bulk $K(\gamma)$ (dashed-dotted line) and shear $\mu(\gamma)$ (solid line) moduli under simple shear for an ensemble of $r_c = 1.2$ glasses. The moduli, whose precise definition is given in Ref. [55], are reported in units of the interatomic interaction energy scale divided by the atomic volume a_0^3. (b) The same as (a), but under hydrostatic tension. (inset) The reduced moduli, $\tilde{\mu}(\epsilon) \equiv \mu(\epsilon)V(\epsilon)/V_0$ and $\tilde{K}(\epsilon) \equiv K(\epsilon)V(\epsilon)/V_0$, under hydrostatic tension (green labels and curve). The corresponding moduli under simple shear (red curves and x label), whose values are identical to those presented in (a) since $V(\gamma) = V_0$, are superimposed for comparison. See text for a discussion of the results.

around a cavitation strain of $\epsilon_c \simeq 0.045$. Second, both moduli significantly soften prior to ϵ_c, where the softening is more pronounced for the bulk modulus.

We note that the expressions for the elastic moduli include an overall factor $1/V$ [55], where V is the current volume. Under simple shear, which is volume preserving, we have $V(\gamma) = V_0$. However, under hydrostatic tension, $V(\epsilon) \geqslant V_0$ is an increasing function of the dilatational strain ϵ. It would be therefore interesting to disentangle the contribution of $1/V(\epsilon)$ to the observed softening under hydrostatic tension from other contributions by defining the reduced moduli, $\tilde{\mu}(\epsilon) \equiv \mu(\epsilon)V(\epsilon)/V_0$ and $\tilde{K}(\epsilon) \equiv K(\epsilon)V(\epsilon)/V_0$. The results are presented in the inset of Fig. 5(b). Interestingly, by superimposing the corresponding moduli under simple shear, which are identical to those presented in Fig. 5(a), it is observed that the reduced shear modulus almost coincides under both loading symmetries, prior to cavitation (in the hydrostatic tension case). On the other hand, the reduced bulk modulus under hydrostatic tension still significantly deviates from its simple shear counterpart, indicating the existence of intrinsic softening processes on top of the varying volume. This observation demonstrates qualitative differences between the shear and bulk moduli.

The softening of the elastic moduli emerges from the accumulation of dilatational plastic deformation and possibly microcavitation in a way that is not yet understood. Understanding these softening processes will also shed light on the qualitative differences between the shear and bulk moduli. More generally, understanding the spatiotemporal dynamics of collective dilatational plasticity upon approaching large-scale cavitation is a challenge for future work.

VI. BRIEF SUMMARY AND OUTLOOK

In this work, we studied elementary processes in glass plasticity, with a focus on dilatational plasticity and its comparison

to its well-studied shear plasticity counterpart. We have extracted, using large-scale AQS computer simulations, the basic micromechanics, geometry and statistical-mechanical properties of unstable plastic modes (zero crossing of an eigenvalue of the glass Hessian) as a function of both the symmetry of the applied driving forces (simple shear versus hydrostatic tension) and the strength of the cohesive/attractive part of the interatomic interaction. These modes feature an effective Eshelby eigenstrain tensor over a spatial scale that defines their plastic core.

In particular, we computed three probability distribution functions of the following quantities: (i) the plastic eigenstrain triaxility R_t (a dimensionless measure of the relative magnitude of the dilatational and deviatoric parts of the eigenstrain tensor), (ii) the planarity ratio R_p (of the deviatoric part of the eigenstrain tensor), and (iii) the linear core size a. We found that R_t strongly depends on the symmetry of the applied driving forces and on the strength of the cohesive/attractive part of the interatomic interaction (Fig. 2). We also found that the deviatoric part of the eigenstrain tensor is generally nonplanar, and that the statistical deviation from planarity is larger for more cohesive/attractive interatomic interactions (Fig. 3). Finally, we found that the statistics of a are almost independent of the symmetry of the applied driving forces, but dependent on the strength of the cohesive/attractive part of the interatomic interaction (Fig. 4). The latter results provide additional support for the intrinsic relations between unstable plastic modes and nonphononic modes in glasses [33,82,83].

At larger scales, involving the collective, spatially-coupled dynamics of many elementary plasticity processes, increasing hydrostatic tension leads to a cavitation instability upon which internal surfaces are formed. Cavity formation is accompanied by a large tension drop, but not an entire loss of load bearing capacity, which persists to larger dilatational strains [Fig. 1(b)]. Interestingly, large-scale cavitation is preceded by a significant softening of the elastic moduli (Fig. 5).

These results open the way for various research directions in dilatational plasticity, which can be roughly classified into two categories. First, additional insight into elementary plasticity processes should be gained. It remains to be understood whether the initial glassy state of disorder, e.g., as controlled by the quench rate through the glass transition temperature, affects the core properties of unstable plastic modes or just their occurrence probability [34].

In this work, we studied unstable plastic modes, which are well-defined micromechanical objects that correspond to saddle points in the glass potential energy landscape. In this context, it is important to better understand both the origin of dilatational plastic instabilities and their outcomes, where the latter constitute the actual contribution to plastic deformation. Preliminary results (not shown here) indicate that the core properties of unstable plastic modes are correlated with the plastic strain accumulated as the glass reaches another potential energy minimum. Future work should systematically explore these correlations. In the context of the origin of plastic instabilities, the relations between quasilocalised, nonphononic modes in glasses (and other structural indicators [33]) to plastic instabilities under hydrostatic tension should be explored. In addition, the emergence of microcavitation, i.e., of particle-scale cavities, should be studied.

Second, at larger scales, future work should address the collective spatiotemporal organization of plastic deformation in glasses in the presence of hydrostatic driving forces, also going beyond the AQS limit (i.e., including finite temperatures and strain rates). These should include the softening of the elastic moduli on the way to cavitation, demonstrated above, as well as large-scale cavity formation and subsequent dynamics. The coupling and competition between shear and dilatational plasticity should be addressed, including the relations and interplay between shear-banding and cavitation (e.g., Ref. [16]). The emerging insight about dilatational plasticity should be eventually incorporated into coarse-grained elasto-plastic models, which will enable to address the fracture toughness of glasses (i.e., irreversible deformation and damage near the edges of crack defects [84,85]) and phenomena such as ductile-to-brittle transitions [16,34,86].

ACKNOWLEDGMENTS

A.M. acknowledges support from the Minerva center on "Aging, from physical materials to human tissues." E.B. acknowledges support from the Ben May Center for Chemical Theory and Computation and the Harold Perlman Family.

APPENDIX: METHODOLOGY

In this Appendix, we describe in more detail the methodology used in this work and the motivation behind it. Additional technical details are offered in Ref. [55]. We employed in this work computer models to address elementary plasticity processes in glasses. Large-scale computer simulations played crucial roles in various recent developments in glass physics (see, for example, Refs. [27,87]). There are multiple reasons for this situation; first, computer glasses provide access to particle-level spatial scales that are essential for understanding glass plasticity, yet they are inaccessible through cutting-edge, real-time experimental techniques.

Second, computer simulations allow to control interatomic interactions in a way that goes well beyond current laboratory techniques. Particularly relevant for understanding dilatational plasticity is the ability to control the strength of the cohesive/attractive part of the interatomic interaction, as noted above. Specifically, we employed potential energy functions $U(\boldsymbol{x})$, where $\boldsymbol{x}$ are the particle coordinates, composed of central force interatomic interactions of the Lennard-Jones type (see detailed formulation in Ref. [55]) in which the cohesive/attractive strength is continuously adjustable, through the dimensionless parameter r_c [55–58] introduced above. The effect of varying r_c on various mesoscopic [57,58] and macroscopic [34] quantities has been recently studied. Among these, we highlighted its effect on the fracture toughness of glasses, where reducing r_c can lead to a ductile-to-brittle transition [34].

Third, computer glass simulations can be performed under athermal quasistatic (AQS) conditions [17–20], corresponding to the zero temperature and strain-rate limits. The AQS protocol is a powerful tool for studying fundamental aspects of the micromechanics, geometry and statistical-mechanical properties of glassy deformation. Its main merit is that it

allows to exhaustively and unambiguously identify discrete plastic processes along the entire deformation path, as done in this work. Finally, computer glasses offer great advantages in implementing the deformation protocols described in Fig. 1. In the context of simple shear deformation, cf. Fig. 1(a), employing periodic boundary conditions allows to eliminate surface effects and hence reach very large strains without failure. Moreover, the hydrostatic tension test, cf. Fig. 1(b), allows to represent a mesoscopic portion of a macroscopic glass that experiences predominantly hydrostatic forces exerted by the surrounding material. We also note in passing that the application of isotropic dilation, which is readily accessible on the computer, is not easy to realize experimentally on the global scale (e.g., compared to the uniaxial tension test [16]), but is feasible (e.g., Ref. [88]).

Glass samples in 3D, each with a fixed number of particles N and initial volume V_0, were generated by rapidly quenching high-temperature, equilibrium binary-mixture liquids into zero temperature inherent states, as detailed in Ref. [55]. While the nonequilibrium thermal history (or more generally thermomechanical history) of a glass has profound implications for its glassy state of disorder (e.g., Ref. [36]), and correspondingly for its material properties—plastic deformability in particular—we did not vary it in this work. It is important to note that our glasses feature vanishingly small initial pressure [as evident in Fig. 1(b)], which for the fixed quenching protocol is achieved by tuning V_0 (at a given N). This is important for revealing the intrinsic dilatational plasticity response of glasses.

Simple shear deformation [cf. Fig. 1(a)] in a given direction is controlled by a shear strain γ. The latter is obtained through the accumulation of AQS strain increments $d\gamma$ [55], for which the deformation gradient tensor $\boldsymbol{F}_{\rm s} = \boldsymbol{\mathcal{I}} + d\gamma\, \hat{\boldsymbol{x}} \otimes \hat{\boldsymbol{y}}$ is applied (here $\boldsymbol{\mathcal{I}}$ is the identity tensor in 3D, $\hat{\boldsymbol{x}}$ and $\hat{\boldsymbol{y}}$ are Cartesian unit vectors, and $\otimes$ is a dyadic/outer product). The stress tensor, and in particular the simple shear stress component $\sigma(\gamma)$, as well as the shear $\mu(\gamma)$ and bulk $K(\gamma)$ moduli, were extracted [55].

Hydrostatic tension [pure dilation, cf. Fig. 1(b)] is controlled by a dilatational (volumetric) strain ϵ. The latter is obtained through the accumulation of AQS strain increments $d\epsilon$ [55], for which the deformation gradient tensor $\boldsymbol{F}_{\rm d} = (1 + d\epsilon)\boldsymbol{\mathcal{I}}$ is applied. The stress tensor, and in particular the hydrostatic tension (negative pressure) $-p(\epsilon)$, as well as the shear $\mu(\epsilon)$ and bulk $K(\epsilon)$ moduli, are extracted.

The potential energy $U(\boldsymbol{x})$ of the glass is minimized during AQS deformation, controlled either by γ or ϵ. As shown above, and consistently with [43], at least part of the plastic deformation in glassy materials—independently of whether obtained under simple shear or hydrostatic tension (or more complex stress states)—occurs through the accumulation of discrete plastic rearrangements (instabilities) that correspond to a zero crossing of an eigenvalue of the Hessian $\boldsymbol{M} \equiv \frac{\partial^2 U}{\partial \boldsymbol{x} \partial \boldsymbol{x}}$ (saddle-node bifurcation [17,19]).

The corresponding particle-level eigenfunctions/eigenmodes $\boldsymbol{u}(\boldsymbol{r})$ (where $\boldsymbol{r}$ is a position vector relative to the center of the eigenmode [55]), is accurately identified and extracted under AQS conditions. The plastic rearrangements (modes) $\boldsymbol{u}(\boldsymbol{r})$ feature a highly-nonlinear, disordered core of linear size a (i.e., of volume $\mathcal{V} \propto a^3$) and a power-law decay $|\boldsymbol{r}|^{-2}$ in the far field (e.g., Ref. [20]), $|\boldsymbol{r}| \gg a$, associated with a linear elastic continuum behavior [89]. The irreversible deformation occurs inside the nonlinear core, whose averaged effect is quantified through an eigenstrain tensor $\boldsymbol{\mathcal{E}}^*$ in the framework of Eshelby's inclusions formalism [59,60].

A recently developed method [61], used in this work, allows to extract $\mathcal{V}\boldsymbol{\mathcal{E}}^*$. Earlier approaches, discussed in the works of [64–66,91] (some of which are discussed above), also invoked Eshelby's inclusions in similar contexts. We note that we analyzed the unstable modes very close to the saddle-node bifurcation, which are well defined mathematical objects, and not the outcome of instability obtained once a new energy minimum is reached. The relation between the two was briefly discussed above. Note also that we considered simple shear and hydrostatic tension as end members of a continuum of stress states, which can be studied as well.

[1] M. A. Meyers and K. K. Chawla, *Mechanical Behavior of Materials* (Cambridge University Press, New York, USA, 2008).

[2] M. F. Ashby, H. Shercliff, and D. Cebon, *Materials: Engineering, Science, Processing and Design* (Butterworth-Heinemann, Cambridge, MA, USA, 2018).

[3] C. Suryanarayana and A. Inoue, *Bulk Metallic Glasses* (CRC press, Boca Raton, 2017).

[4] W. H. Wang, C. Dong, and C. Shek, Bulk metallic glasses, Mater. Sci. Eng.: R: Rep. **44**, 45 (2004).

[5] L. Wondraczek, E. Bouchbinder, A. Ehrlicher, J. C. Mauro, R. Sajzew, and M. M. Smedskjaer, Advancing the mechanical performance of glasses: Perspectives and challenges, Adv. Mater. **34**, 2109029 (2022).

[6] J. Schroers, Processing of bulk metallic glass, Adv. Mater. **22**, 1566 (2010).

[7] G. Wang, D. Zhao, H. Bai, M. Pan, A. Xia, B. Han, X. Xi, Y. Wu, and W. Wang, Nanoscale periodic morphologies on the fracture surface of Brittle metallic glasses, Phys. Rev. Lett. **98**, 235501 (2007).

[8] M. Jiang, Z. Ling, J. Meng, and L. Dai, Energy dissipation in fracture of bulk metallic glasses via inherent competition between local softening and quasi-cleavage, Philos. Mag. **88**, 407 (2008).

[9] M. Jiang, G. Wilde, J. Chen, C. Qu, S. Fu, F. Jiang, and L. Dai, Cryogenic-temperature-induced transition from shear to dilatational failure in metallic glasses, Acta Mater. **77**, 248 (2014).

[10] E. Bouchaud, D. Boivin, J. L. Pouchou, D. Bonamy, B. Poon, and G. Ravichandran, Fracture through cavitation in a metallic glass, Europhys. Lett. **83**, 66006 (2008).

[11] Y. Shao, G. N. Yang, K. F. Yao, and X. Liu, Direct experimental evidence of nano-voids formation and coalescence within shear bands, Appl. Phys. Lett. **105**, 181909 (2014).

[12] R. Narasimhan, P. Tandaiya, I. Singh, R. Narayan, and U. Ramamurty, Fracture in metallic glasses: Mechanics and mechanisms, Int. J. Fract. **191**, 53 (2015).

[13] I. Singh, R. Narasimhan, and U. Ramamurty, Cavitation-induced fracture causes nanocorrugations in

brittle metallic glasses, Phys. Rev. Lett. **117**, 044302 (2016).
[14] Q. An, K. Samwer, M. D. Demetriou, M. C. Floyd, D. O. Duggins, W. L. Johnson, and W. A. Goddard III, How the toughness in metallic glasses depends on topological and chemical heterogeneity, Proc. Natl. Acad. Sci. USA **113**, 7053 (2016).
[15] L. Q. Shen, J. H. Yu, X. C. Tang, B. A. Sun, Y. H. Liu, H. Y. Bai, and W. H. Wang, Observation of cavitation governing fracture in glasses, Sci. Adv. **7**, eabf7293 (2021).
[16] D. Richard, E. T. Lund, J. Schroers, and E. Bouchbinder, Bridging necking and shear-banding mediated tensile failure in glasses, Phys. Rev. Mater. **7**, L032601 (2023).
[17] D. L. Malandro and D. J. Lacks, Relationships of shear-induced changes in the potential energy landscape to the mechanical properties of ductile glasses, J. Chem. Phys. **110**, 4593 (1999).
[18] C. Maloney and A. Lemaitre, Subextensive scaling in the athermal, quasistatic limit of amorphous matter in plastic shear flow, Phys. Rev. Lett. **93**, 016001 (2004).
[19] C. E. Maloney and D. J. Lacks, Energy barrier scalings in driven systems, Phys. Rev. E **73**, 061106 (2006).
[20] C. E. Maloney and A. Lemaître, Amorphous systems in athermal, quasistatic shear, Phys. Rev. E **74**, 016118 (2006).
[21] A. Tanguy, F. Leonforte, and J. L. Barrat, Plastic response of a 2D Lennard-Jones amorphous solid: Detailed analysis of the local rearrangements at very slow strain rate, Eur. Phys. J. E **20**, 355 (2006).
[22] A. Lemaître and C. Caroli, Rate-dependent avalanche size in athermally sheared amorphous solids, Phys. Rev. Lett. **103**, 065501 (2009).
[23] S. Karmakar, E. Lerner, and I. Procaccia, Athermal nonlinear elastic constants of amorphous solids, Phys. Rev. E **82**, 026105 (2010).
[24] M. Tsamados, A. Tanguy, C. Goldenberg, and J. L. Barrat, Local elasticity map and plasticity in a model Lennard-Jones glass, Phys. Rev. E **80**, 026112 (2009).
[25] S. Karmakar, E. Lerner, and I. Procaccia, Statistical physics of the yielding transition in amorphous solids, Phys. Rev. E **82**, 055103(R) (2010).
[26] S. Karmakar, E. Lerner, I. Procaccia, and J. Zylberg, Statistical physics of elastoplastic steady states in amorphous solids: Finite temperatures and strain rates, Phys. Rev. E **82**, 031301 (2010).
[27] M. Falk and C. Maloney, Simulating the mechanical response of amorphous solids using atomistic methods, Eur. Phys. J. B **75**, 405 (2010).
[28] D. Rodney, A. Tanguy, and D. Vandembroucq, Modeling the mechanics of amorphous solids at different length scale and time scale, Modell. Simul. Mater. Sci. Eng. **19**, 083001 (2011).
[29] K. M. Salerno, C. E. Maloney, and M. O. Robbins, Avalanches in strained amorphous solids: Does inertia destroy critical behavior?, Phys. Rev. Lett. **109**, 105703 (2012).
[30] T. C. Hufnagel, C. A. Schuh, and M. L. Falk, Deformation of metallic glasses: Recent developments in theory, simulations, and experiments, Acta Mater. **109**, 375 (2016).
[31] C. Liu, E. E. Ferrero, F. Puosi, J. L. Barrat, and K. Martens, Driving rate dependence of avalanche statistics and shapes at the yielding transition, Phys. Rev. Lett. **116**, 065501 (2016).
[32] M. Ozawa, L. Berthier, G. Biroli, A. Rosso, and G. Tarjus, Random critical point separates brittle and ductile yielding transitions in amorphous materials, Proc. Natl. Acad. Sci. USA **115**, 6656 (2018).
[33] D. Richard, M. Ozawa, S. Patinet, E. Stanifer, B. Shang, S. Ridout, B. Xu, G. Zhang, P. Morse, J. L. Barrat *et al.*, Predicting plasticity in disordered solids from structural indicators, Phys. Rev. Mater. **4**, 113609 (2020).
[34] D. Richard, E. Lerner, and E. Bouchbinder, Brittle-to-ductile transitions in glasses: Roles of soft defects and loading geometry, MRS Bull. **46**, 902 (2021).
[35] G. Kapteijns, E. Bouchbinder, and E. Lerner, Unified quantifier of mechanical disorder in solids, Phys. Rev. E **104**, 035001 (2021).
[36] K. González-López, E. Bouchbinder, and E. Lerner, Variability of mesoscopic mechanical disorder in disordered solids, J. Non-Cryst. Solids **604**, 122137 (2023).
[37] Q. An, G. Garrett, K. Samwer, Y. Liu, S. V. Zybin, S. N. Luo, M. D. Demetriou, W. L. Johnson, and W. A. Goddard III, Atomistic characterization of stochastic cavitation of a binary metallic liquid under negative pressure, J. Phys. Chem. Lett. **2**, 1320 (2011).
[38] P. Murali, T. Guo, Y. Zhang, R. Narasimhan, Y. Li, and H. Gao, Atomic scale fluctuations govern brittle fracture and cavitation behavior in metallic glasses, Phys. Rev. Lett. **107**, 215501 (2011).
[39] P. Guan, S. Lu, M. J. Spector, P. K. Valavala, and M. L. Falk, Cavitation in amorphous solids, Phys. Rev. Lett. **110**, 185502 (2013).
[40] P. Chaudhuri and J. Horbach, Structural inhomogeneities in glasses via cavitation, Phys. Rev. B **94**, 094203 (2016).
[41] K. Paul, R. Dasgupta, J. Horbach, and S. Karmakar, Cavity formation in deformed amorphous solids on the nanoscale, Phys. Rev. Res. **2**, 042012 (2020).
[42] M. Shimada and N. Oyama, Gas-liquid phase separation at zero temperature: mechanical interpretation and implications for gelation, Soft Matter **18**, 8406 (2022).
[43] U. A. Dattani, S. Karmakar, and P. Chaudhuri, Universal mechanical instabilities in the energy landscape of amorphous solids: Evidence from athermal quasistatic expansion, Phys. Rev. E **106**, 055004 (2022).
[44] U. A. Dattani, R. Sharma, S. Karmakar, and P. Chaudhuri, Cavitation instabilities in amorphous solids via secondary mechanical perturbations, arXiv:2303.04529.
[45] U. A. Dattani, S. Karmakar, and P. Chaudhuri, Athermal quasistatic cavitation in amorphous solids: Effect of random pinning, arXiv:2306.05348.
[46] A. S. Argon, Plastic deformation in metallic glasses, Acta Metall. **27**, 47 (1979).
[47] S. Kobayashi, K. Maeda, and S. Takeuchi, Computer simulation of deformation of amorphous $Cu_{57}Zr_{43}$, Acta Metall. **28**, 1641 (1980).
[48] K. Maeda and S. Takeuchi, Atomistic process of plastic deformation in a model amorphous metal, Philos. Mag. A **44**, 643 (1981).
[49] M. L. Falk and J. S. Langer, Dynamics of viscoplastic deformation in amorphous solids, Phys. Rev. E **57**, 7192 (1998).
[50] Y. J. Wang, M. Jiang, Z. Tian, and L. Dai, Direct atomic-scale evidence for shear-dilatation correlation in metallic glasses, Scr. Mater. **112**, 37 (2016).

[51] Y. Shi, J. Luo, F. Yuan, and L. Huang, Intrinsic ductility of glassy solids, J. Appl. Phys. **115**, 043528 (2014).

[52] L. Sun, M. Jiang, and L. Dai, Intrinsic correlation between dilatation and pressure sensitivity of plastic flow in metallic glasses, Scr. Mater. **63**, 945 (2010).

[53] X. Huang, Z. Ling, and L. Dai, Ductile-to-brittle transition in spallation of metallic glasses, J. Appl. Phys. **116**, 143503 (2014).

[54] Y. Chen, M. Jiang, Y. Wei, and L. Dai, Failure criterion for metallic glasses, Philos. Mag. **91**, 4536 (2011).

[55] See Supplemental Material at http://link.aps.org/supplemental/10.1103/PhysRevResearch.6.023167 for additional technical details, which includes Refs. [56–58,61,82,92–102].

[56] S. Karmakar, E. Lerner, I. Procaccia, and J. Zylberg, Effect of the interparticle potential on the yield stress of amorphous solids, Phys. Rev. E **83**, 046106 (2011).

[57] K. González-López, M. Shivam, Y. Zheng, M. P. Ciamarra, and E. Lerner, Mechanical disorder of sticky-sphere glasses. I. Effect of attractive interactions, Phys. Rev. E **103**, 022605 (2021).

[58] K. González-López, M. Shivam, Y. Zheng, M. P. Ciamarra, and E. Lerner, Mechanical disorder of sticky-sphere glasses. II. Thermomechanical inannealability, Phys. Rev. E **103**, 022606 (2021).

[59] J. D. Eshelby, The determination of the elastic field of an ellipsoidal inclusion, and related problems, Proc. Math. Phys. Eng. Sci. **241**, 376 (1957).

[60] J. D. Eshelby, The elastic field outside an ellipsoidal inclusion, Proc. Math. Phys. Eng. Sci. **252**, 561 (1959).

[61] A. Moriel, Y. Lubomirsky, E. Lerner, and E. Bouchbinder, Extracting the properties of quasilocalized modes in computer glasses: Long-range continuum fields, contour integrals, and boundary effects, Phys. Rev. E **102**, 033008 (2020).

[62] E. Davis and F. Connelly, Stress distribution and plastic deformation in rotating cylinders of strain-hardening material, J. Appl. Mech. **26**, 25 (1959).

[63] S. Murakami, *Continuum Damage Mechanics: a Continuum Mechanics Approach to the Analysis of Damage and Fracture* (Springer Science & Business Media, New York, USA, 2012), Vol. 125.

[64] Ashwin J., O. Gendelman, I. Procaccia, and C. Shor, Yield-strain and shear-band direction in amorphous solids under two-dimensional uniaxial loading, Phys. Rev. E **88**, 022310 (2013).

[65] A. Nicolas and J. Rottler, Orientation of plastic rearrangements in two-dimensional model glasses under shear, Phys. Rev. E **97**, 063002 (2018).

[66] T. Albaret, A. Tanguy, F. Boioli, and D. Rodney, Mapping between atomistic simulations and Eshelby inclusions in the shear deformation of an amorphous silicon model, Phys. Rev. E **93**, 053002 (2016).

[67] F. H. Stillinger and T. A. Weber, Computer simulation of local order in condensed phases of silicon, Phys. Rev. B **31**, 5262 (1985).

[68] D. Holland and M. Marder, Ideal brittle fracture of silicon studied with molecular dynamics, Phys. Rev. Lett. **80**, 746 (1998).

[69] D. Holland and M. Marder, Cracks and atoms, Adv. Mater. **11**, 793 (1999).

[70] R. Dasgupta, O. Gendelman, P. Mishra, I. Procaccia, and C. A. B. Z. Shor, Shear localization in three-dimensional amorphous solids, Phys. Rev. E **88**, 032401 (2013).

[71] D. Pan, Y. Yokoyama, T. Fujita, Y. Liu, S. Kohara, A. Inoue, and M. Chen, Correlation between structural relaxation and shear transformation zone volume of a bulk metallic glass, Appl. Phys. Lett. **95**, 141909 (2009).

[72] F. Jiang, M. Jiang, H. Wang, Y. Zhao, L. He, and J. Sun, Shear transformation zone volume determining Ductile-Brittle transition of bulk metallic glasses, Acta Mater. **59**, 2057 (2011).

[73] Z. Chen, L. Huang, P. Huang, K. Xu, F. Wang, and T. Lu, Clarification on shear transformation zone size and its correlation with plasticity for Zr-based bulk metallic glass in different structural states, Mater. Sci. Eng.: A **677**, 349 (2016).

[74] R. Bell and P. Dean, Atomic vibrations in vitreous silica, Discuss. Faraday Soc. **50**, 55 (1970).

[75] R. Bell, The dynamics of disordered lattices, Rep. Prog. Phys. **35**, 1315 (1972).

[76] D. Pan, A. Inoue, T. Sakurai, and M. W. Chen, Experimental characterization of shear transformation zones for plastic flow of bulk metallic glasses, Proc. Natl. Acad. Sci. USA **105**, 14769 (2008).

[77] E. Lerner, G. Düring, and E. Bouchbinder, Statistics and properties of low-frequency vibrational modes in structural glasses, Phys. Rev. Lett. **117**, 035501 (2016).

[78] H. Mizuno, H. Shiba, and A. Ikeda, Continuum limit of the vibrational properties of amorphous solids, Proc. Natl. Acad. Sci. USA **114**, E9767 (2017).

[79] G. Kapteijns, E. Bouchbinder, and E. Lerner, Universal nonphononic density of states in 2D, 3D, and 4D glasses, Phys. Rev. Lett. **121**, 055501 (2018).

[80] L. Wang, A. Ninarello, P. Guan, L. Berthier, G. Szamel, and E. Flenner, Low-frequency vibrational modes of stable glasses, Nat. Commun. **10**, 26 (2019).

[81] D. Richard, K. González-López, G. Kapteijns, R. Pater, T. Vaknin, E. Bouchbinder, and E. Lerner, Universality of the nonphononic vibrational spectrum across different classes of computer glasses, Phys. Rev. Lett. **125**, 085502 (2020).

[82] E. Lerner and E. Bouchbinder, Low-energy quasilocalized excitations in structural glasses, J. Chem. Phys. **155**, 200901 (2021).

[83] J. Zylberg, E. Lerner, Y. Bar-Sinai, and E. Bouchbinder, Local thermal energy as a structural indicator in glasses, Proc. Natl. Acad. Sci. USA **114**, 7289 (2017).

[84] C. H. Rycroft and E. Bouchbinder, Fracture toughness of metallic glasses: Annealing-induced embrittlement, Phys. Rev. Lett. **109**, 194301 (2012).

[85] M. Vasoya, C. H. Rycroft, and E. Bouchbinder, Notch fracture toughness of glasses: Dependence on rate, age, and geometry, Phys. Rev. Appl. **6**, 024008 (2016).

[86] J. Ketkaew, W. Chen, H. Wang, A. Datye, M. Fan, G. Pereira, U. D. Schwarz, Z. Liu, R. Yamada, W. Dmowski *et al.*, Mechanical glass transition revealed by the fracture toughness of metallic glasses, Nat. Commun. **9**, 3271 (2018).

[87] A. Ninarello, L. Berthier, and D. Coslovich, Models and algorithms for the next generation of glass transition studies, Phys. Rev. X **7**, 021039 (2017).

[88] A. Dorfmann, Stress softening of elastomers in hydrostatic tension, Acta Mech. **165**, 117 (2003).

[89] We note that in certain limiting cases, e.g., related to the jamming point, the core can be extended and feature a power-law decay of its own, see Ref. [90].
[90] E. Lerner and E. Bouchbinder, Anomalous linear elasticity of disordered networks, Soft Matter **19**, 1076 (2023).
[91] F. Boioli, T. Albaret, and D. Rodney, Shear transformation distribution and activation in glasses at the atomic scale, Phys. Rev. E **95**, 033005 (2017).
[92] J. Chattoraj and M. P. Ciamarra, Role of attractive forces in the relaxation dynamics of supercooled liquids, Phys. Rev. Lett. **124**, 028001 (2020).
[93] H. J. C. Berendsen, J. P. M. Postma, W. F. van Gunsteren, A. DiNola, and J. R. Haak, Molecular dynamics with coupling to an external bath, J. Chem. Phys. **81**, 3684 (1984).
[94] M. P. Allen and D. J. Tildesley, *Computer Simulation of Liquids* (Oxford University Press, Oxford, UK, 2017).
[95] W. Ji, M. Popović, T. W. J. de Geus, E. Lerner, and M. Wyart, Theory for the density of interacting quasilocalized modes in amorphous solids, Phys. Rev. E **99**, 023003 (2019).
[96] S. Wijtmans and M. L. Manning, Disentangling defects and sound modes in disordered solids, Soft Matter **13**, 5649 (2017).
[97] G. Kapteijns, D. Richard, and E. Lerner, Nonlinear quasilocalized excitations in glasses: True representatives of soft spots, Phys. Rev. E **101**, 032130 (2020).
[98] E. Lerner, Micromechanics of nonlinear plastic modes, Phys. Rev. E **93**, 053004 (2016).
[99] L. Gartner and E. Lerner, Nonlinear modes disentangle glassy and Goldstone modes in structural glasses, SciPost Phys. **1**, 016 (2016).
[100] J. F. Lutsko, Generalized expressions for the calculation of elastic constants by computer simulation, J. Appl. Phys. **65**, 2991 (1989).
[101] M. A. Blanco, M. Flórez, and M. Bermejo, Evaluation of the rotation matrices in the basis of real spherical harmonics, J. Mol. Struct. (THEOCHEM) **419**, 19 (1997).
[102] C. D. H. Chisholm, *Group Theoretical Techniques in Quantum Chemistry* (Academic Press, New York, 1976).